IOP Publishing Superconductor Science and Technology
Supercond. Sci. Technol. **28** (2015) 095010 (8pp) doi:10.1088/0953-2048/28/9/095010

A gradient coil design for a high-temperature superconducting bulk magnet using the finite-difference method

D Tamada[1,2], T Nakamura[1,2] and K Kose[1]

[1] Institute of Applied Physics, University of Tsukuba, 1-1-1 Tennodai, Tsukuba, Ibaraki, 305-8573, Japan
[2] RIKEN, 2-1 Hirosawa, Wako, Saitama, 351-0198, Japan

E-mail: tamada@mrlab.frsc.tsukuba.ac.jp

Received 1 April 2015, revised 14 June 2015
Accepted for publication 28 June 2015
Published 27 July 2015

Abstract

The screening current induced in a bulk superconductor presents a critical problem for gradient coil design because it gives rise to undesirable effects on the gradient field: namely, a decrease in the efficiency and a distortion of the field. In this paper, a new coil design method for the bulk magnet is proposed using the finite-difference method (FDM) and the target-field method. The calculation using the FDM was implemented with the boundary conditions of the bulk magnet. Transverse and longitudinal coils were designed and fabricated for a high-temperature superconducting bulk magnet. The calculated results of the efficiency and the nonlinearity distribution of the gradient field agreed well with the measured results.

Keywords: magnetic resonance imaging, gradient coil, screening current, high-temperature superconducting bulk magnet

1. Introduction

A strong and stable magnetic field is required to polarize the nuclear spins for nuclear magnetic resonance (NMR) and magnetic resonance imaging (MRI). In most cases, NbTi superconducting magnets are used to generate the magnetic field. Recently, high-temperature superconducting magnets [1–5] have received increased attention because of recent helium shortages.

A high-temperature superconducting (HTS) bulk magnet is a promising magnet for NMR/MRI [4, 5]. In 2011, Ogawa *et al* demonstrated MRI using a bulk magnet comprised of YBCO bulk superconductors (critical temperature $T_c = 92$ K) operated at 4.7 T without liquid helium [5]. In that paper, they showed the feasibility of the magnet by performing imaging experiments with a voxel size of 50 μm^3.

Recently, some papers have addressed a problem concerning the fact that the magnetic field induced by shim and gradient coils comes to be shielded as a result of the Meissner effect [6–9]. In 2009, Harn *et al* reported that the field induced by superconducting shim coils installed outside the HTS magnet using $(Bi,Pb)_2Sr_2Ca_2Cu_3O_y$ (Bi2223) superconductor tapes was distorted by the shielding current [6]. In this paper, significant degradation of the current efficiency in shim coils and unexpected nonlinear behavior of shim ciols were observed. The degradation of the efficiency in shim coils with the $(RE)Ba_2Cu_3O_{7x}$ NMR magnet was also reported by Yanagisawa *et al* in 2014 [7]. To reduce the degradation of the shim coil's performance, Ahn proposed to use room temperature (RT) shim coils installed inside the HTS magnet using $GdBa_2Cu_3O_7$ (GdBCO)-coated conductor tapes [8]. In 2013, we reported on the shielding effect on gradient coils installed in the RT bore of the bulk magnet, as well as on the magnet using HTS tapes [9]. In this paper, the decrease of current efficiency of the gradient coils was observed when the bulk magnet was cooled below T_c.

When a type-II superconductor such as YBCO is cooled below T_c, the magnetic flux below the lower critical field is expelled as a result of the Meissner effect. As a result, the shielding current (also called the screening current) is induced on the surface of the bulk superconductor to cancel the flux inside [10, 11]. Therefore, the flux induced by the gradient and shim coils is distorted. In this case, it becomes difficult to design the gradient coil patterns in such a way as to generate the target gradient field.

Gradient coils must be designed so as to generate a desired linear field gradient in the *x*-, *y*-, and *z*-directions. The nonlinearity of the gradient field gives rise to distortion in the acquired MR images. Furthermore, the magnitude of the gradient is also an important factor in determining the resolution of the images. These factors are in a trade-off relationship with each other; therefore, a large number of studies have been performed on the gradient coil [12]. However, no study has ever tried to develop the gradient coil for an HTS magnet, such as the bulk magnet, because of the shielding effect mentioned above.

In this paper, we propose a new gradient coil design approach using the target-field method [12–17] and the finite-difference method (FDM) [18, 19] for the bulk magnet. An imaging experiment using a lattice phantom is performed with the gradient coil designed in this study to demonstrate the validity of our approach.

2. Theory

In this study, the current density of the gradient coil is assumed to be the linear combination of the set of square currents. Then, the combination coefficients will be obtained using the target-field method. The magnetic field distributions produced by the square currents can be calculated using the FDM to consider the shielding effect, as described in section 2.2.

To evaluate the gradient coil performance, the gradient field was measured using the phantom-based method. The gradient field can be estimated from the pixel distortion in the MR image acquired using the designed gradient coils, as described in section 2.3.

2.1. Target-field method

The target-field method is one of the design methods for the gradient coil; it was first proposed by Turner [12, 13]. The main problem associated with this approach is that it is difficult to design a current density distribution on a finite region, because a Fourier transform is required to derive the current distribution of a coil. There is no guarantee that the distribution will converge on the desired finite region. In this case, it becomes difficult to fabricate the coil [14–16]. To overcome this problem, a method based on the linear combination of finite Fourier series was proposed [16, 17].

In this study, the current density for the gradient coil was derived using the linear combination of the set of square currents on the cylindrical surface, as shown in figure 1, which are not orthogonal to each other. At first, the magnetic field distributions $\mathbf{Q_n}$ induced by the square currents $\mathbf{J_n}$—which are smoothed by convolution with Gaussian kernels—were calculated using the FDM (see section 2.2). At this stage, the magnetic field $\mathbf{B}_s$ induced by the gradient coil can be expressed as follows:

$$\mathbf{B}_s = \sum_i^n c_i \mathbf{Q}_i, \tag{1}$$

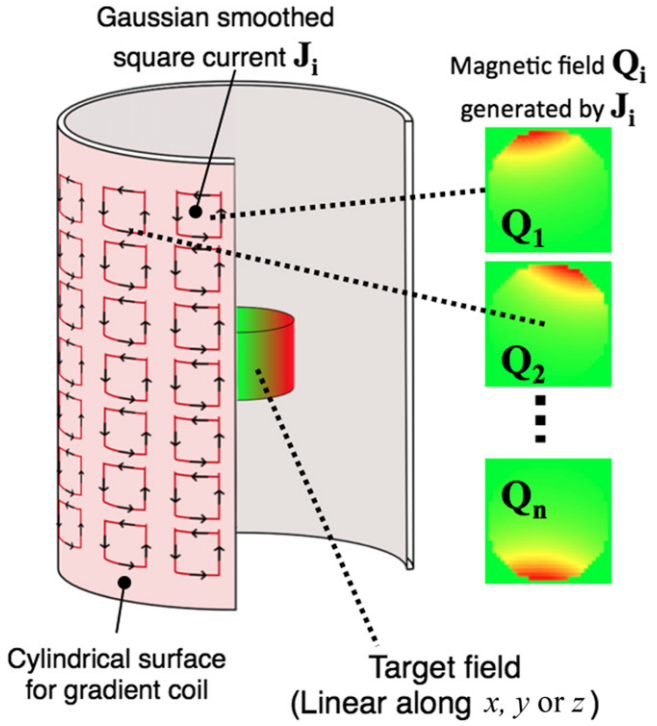

Figure 1. The set of square currents for the cylindrical gradient coil.

where c_n denotes the linear combination coefficients. Ideally, the target field $\mathrm{B}^{(t)}$ is equal to B_s as follows:

$$\begin{aligned}\mathbf{B}_s = \quad & \mathbf{B}^{(t)} \\ = & \sum_i^n c_i \mathbf{Q}_i.\end{aligned} \tag{2}$$

Equation (10) can be written in matrix form as:

$$\begin{bmatrix} B_1^{(t)} \\ B_2^{(t)} \\ \vdots \\ B_n^{(t)} \end{bmatrix} = \begin{bmatrix} Q_{11} & Q_{12} & \cdots & Q_{1n} \\ Q_{21} & Q_{22} & \cdots & Q_{2n} \\ \vdots & \vdots & \ddots & \vdots \\ Q_{m1} & Q_{m2} & \cdots & Q_{mn} \end{bmatrix} \begin{bmatrix} c_1 \\ c_2 \\ \vdots \\ c_n \end{bmatrix}, \tag{3}$$

where ${B_m}^{(t)}$ and Q_{mn} denote the values of $B^{(t)}$ and $\boldsymbol{Q}_{\mathbf{m}}$ at the mth point. In this case, c_n can be obtained by calculating the inverse matrix of $\boldsymbol{Q}_{\mathbf{m}}$ as follows:

$$\begin{bmatrix} c_1 \\ c_2 \\ \vdots \\ c_n \end{bmatrix} = \begin{bmatrix} Q_{11} & Q_{12} & \cdots & Q_{1n} \\ Q_{21} & Q_{22} & \cdots & Q_{2n} \\ \vdots & \vdots & \ddots & \vdots \\ Q_{m1} & Q_{m2} & \cdots & Q_{mn} \end{bmatrix}^{-1} \begin{bmatrix} B_1^{(t)} \\ B_2^{(t)} \\ \vdots \\ B_n^{(t)} \end{bmatrix}. \tag{4}$$

However, in the case of $\mathrm{m} > \mathrm{n}$, the equation represents an ill-posed problem and must be solved using Tikhonov regularization as follows:

$$F = \left\| \mathbf{B}_t - \sum_i^n c_i \mathbf{Q}_i \right\|^2 + \alpha ||c||^2, \tag{5}$$

where α is the regularization parameter and $\|^2$ denotes the L2 norm operator. The current density J_s of the gradient coil can be expressed as follows:

$$\mathbf{J}_s = \sum_i^n c_i \mathbf{J}_i. \tag{6}$$

Finally, the winding pattern can be obtained by using the stream function method [12]. Because the current density of the coil is continuous, as expressed in equation (7), there exists a stream function S that represents the streamlines of current flow:

$$\nabla \cdot \mathbf{J}_s = \mathbf{0}. \tag{7}$$

Therefore, S can be expressed as follows:

$$J_s^{(z)} = \frac{\partial S}{\partial \phi}, \tag{8}$$

where $J_s^{(z)}$ is the z-component of $\mathbf{J_s}$. Finally, S can be derived by solving the integral below:

$$S = \int_{-\pi}^{\pi} J_s^{(x)} \mathrm{d}\phi. \tag{9}$$

The winding patterns are then approximated as contour lines of S.

2.2. Magnetic field calculation using the finite-difference method

There are some approaches, such as the finite-element method and boundary-element method, to estimate the current density distributions for gradient coils. The FDM-based method was first proposed by Zhu *et al* to achieve flexible and straightforward coil optimization. In this study, we used the FDM approach to consider the Meissner effect.

Figure 2 shows the boundary conditions and the geometric condition of the square currents used for the FDM calculation.

In this study, gradient coils are located in the RT bore of the bulk magnet. Therefore, the vector potential $\boldsymbol{A_i}$ and the magnetic field $\boldsymbol{Q_i}$ generated by the square current at the ith position and the boundary conditions can be expressed by the following equations:

$$\begin{aligned} \nabla^2 \mathbf{A}_i &= \begin{cases} -\mu_0 \mathbf{J}_i \left(r < R_1\right) \\ -\mu_1 \mathbf{J}_i \left(R_1 < r < R_2\right) \end{cases} \\ \nabla \times \mathbf{A}_i &= 0 \left(R_1 < r < R_2\right) \\ \mathbf{Q}_i &= 0 \left(R_1 < r < R_2\right), \end{aligned} \tag{10}$$

where R_1 and R_2 denote the inner and outer radii of the bulk superconductors from the z-axis, $\mathbf{J_i}$ denotes the current density distribution of the square currents in the bulk magnet, and μ_0 and μ_1 denote the permeability of free space and of the superconductors, respectively. However, it is complicated to solve the above equations when taking into consideration the Neumann boundary condition. In this study, we assumed that

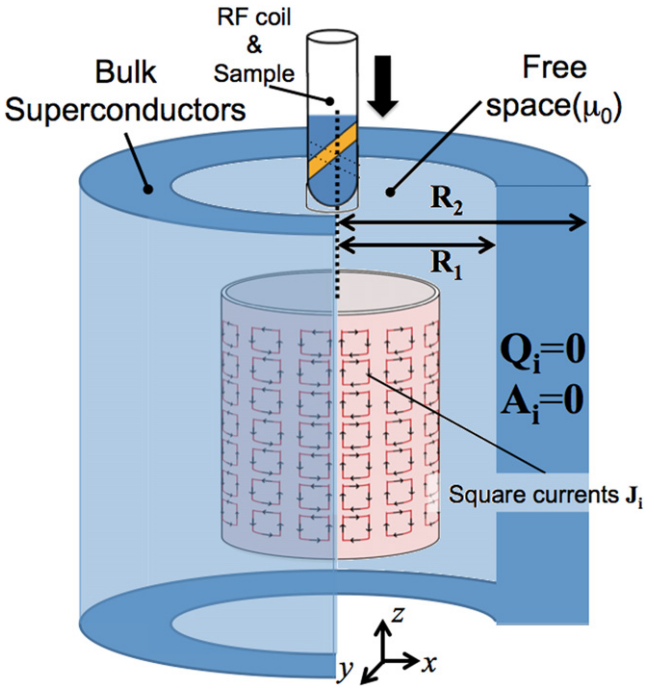

Figure 2. The boundary conditions used in this study.

the London penetration depth (typically, a few hundred nanometers) is much smaller than the thickness of the bulk magnet ($R_2 - R_1$). Moreover, the bulk superconductors can be assumed to be uniform materials whose μ_1 is zero. Therefore, the boundary conditions can be expressed as follows:

$$\begin{aligned} \nabla^2 \mathbf{A}_i &= \left\{ -\mu_0 \mathbf{J}_i \left(r < R_1\right) 0 \left(R_1 < r < R_2\right) \right. \\ \mathbf{A}_i &= 0 \left(R_1 < r < R_2\right) \\ \mathbf{Q}_i &= 0 \left(R_1 < r < R_2\right). \end{aligned} \tag{11}$$

In this study, this equation was solved using the FDM.

The magnetic vector potential $\mathbf{A_i}$ in the free space can be defined as follows:

$$\begin{aligned} \nabla^2 \mathbf{A}_i &= -\mu_0 \mathbf{J}_i \\ \mathbf{Q}_i &= \nabla \times \mathbf{A}_i. \end{aligned} \tag{12}$$

When the z-axis is parallel to the main field of the magnet, the x- and y-components of $\mathbf{A}_i$ must be obtained in order to derive the z-component of $\mathbf{Q}_i$ by solving the following equations:

$$\begin{aligned} \nabla^2 A_{ix} &= -\mu_0 j_{ix} \\ \nabla^2 A_{iy} &= -\mu_0 j_{iy}, \end{aligned} \tag{13}$$

where A_{ix} and A_{iy} are the x- and y-components of $\mathbf{A_i}$, and j_{ix} and j_{iy} are the x- and y-components of $\mathbf{J_i}$.

At this stage, these equations are discretized according to the definition of the partial derivative, given below:

$$\frac{\partial A_{ix}}{\partial x} \equiv \lim_{\Delta \to 0} \frac{A_{ix}(x, y, z) - A_{ix}(x - \Delta, y, z)}{\Delta}. \tag{14}$$

The second derivative of A_{ix} is defined as follows:

$$\frac{\partial^2 A_{ix}}{\partial x^2} \equiv \lim_{\Delta \to 0}\Big(\big(A_{ix}(x-\Delta, y, z) + A_{ix}(x+\Delta, y, z) - 2A_{ix}(x, y, z)\big)\big/\Delta^2\Big). \quad (15)$$

The second derivative can be approximated with the following equations:

$$\begin{aligned}\frac{\partial^2 A_{ix}}{\partial x^2} + \frac{\partial^2 A_{iy}}{\partial y^2} + \frac{\partial^2 A_{iz}}{\partial z^2} \approx{}& \Big(\big(A_{ix}(x-\Delta, y, z) \\ &+ A_{ix}(x+\Delta, y, z) - 2A_{ix}(x, y, z)\big)\big/\Delta^2\Big) \\ &+ \Big(\big(A_{iy}(x, y-\Delta, z) + A_{iy}(x, y+\Delta, z) \\ &- 2A_{iy}(x, y, z)\big)\big/\Delta^2\Big) \\ &+ \Big(\big(A_{iz}(x, y, z-\Delta) + A_{iz}(x, y, z+\Delta) \\ &- 2A_{iz}(x, y, z)\big)\big/\Delta^2\Big). \end{aligned} \quad (16)$$

The vector potentials can be solved using the linear iterative method [18], given by:

$$\begin{aligned}A_{ix}^{(k+1)}(x, y, z) = \frac{1}{6}\Big[&\mu_0\Delta^2 j_{ix} + A_{ix}^{(k)}(x+1, y, z) \\ &+ A_{ix}^{(k+1)}(x-1, y, z) + A_{ix}^{(k)}(x, y+1, z) + A_{ix}^{(k+1)} \\ &\times (x, y-1, z) + A_{ix}^{(k)}(x, y, z+1) + A_{ix}^{(k+1)} \\ &\times (x, y, z-1)\Big] \\ A_{iy}^{(k+1)}(x, y, z) = \frac{1}{6}\Big[&\mu_0\Delta^2 j_{iy} + A_{iy}^{(k)}(x+1, y, z) \\ &+ A_{iy}^{(k+1)}(x-1, y, z) + A_{iy}^{(k)}(x, y+1, z) + A_{iy}^{(k+1)} \\ &\times (x, y-1, z) + A_{iy}^{(k)}(x, y, z+1) + A_{iy}^{(k+1)} \\ &\times (x, y, z-1)\Big], \end{aligned} \quad (17)$$

where $A_{ix}^{(k)}$ and $A_{iy}^{(k)}$ are the successive approximations at iteration k. The iteration is stopped if the maximum values of $\left|A_{ix}^{(k+1)} - A_{ix}^{(k)}\right|$ and $\left|A_{iy}^{(k+1)} - A_{iy}^{(k)}\right|$ are less than the tolerance. Finally, $\mathbf{Q_i}$ can be obtained by using equation (12).

2.3. Gradient field estimation using the lattice phantom

The magnetic field induced by the gradient coil was estimated by using the phantom-based method [20, 21]. The gradient fields G_x, G_y, and G_z induced by the x-, y-, and z-gradient coils at the spatial coordinates (x, y, z) are defined as follows:

$$\begin{aligned}G_x(x, y, z) &= g_x x + \Delta g_x(x, y, z) \\ G_y(x, y, z) &= g_y y + \Delta g_y(x, y, z) \\ G_z(x, y, z) &= g_z z + \Delta g_z(x, y, z), \end{aligned} \quad (18)$$

where g_x, g_y, and g_z are the field gradients for the x-, y-, and z-gradient coils, respectively; Δg_x, Δg_y, and Δg_z are the nonlinear components of the field induced by the x-, y-, and z-gradient coils, respectively.

The coordinates (u, v, w) in the MR image with the readout gradient along the z-axis can be expressed as follows:

$$\begin{aligned}u &= x + \frac{\Delta g_x(x, y, z)}{g_x} \\ v &= y + \frac{\Delta g_y(x, y, z)}{g_y} \\ w &= z + \frac{\Delta g_z(x, y, z) + \Delta B_0}{g_z}, \end{aligned} \quad (19)$$

where ΔB_0 is the inhomogeneity of the magnetic field.

The nonlinear components of the gradient field along the phase-encoding direction can be obtained by calculating the distortion of the MR image as follows:

$$\begin{aligned}\Delta g_x(x, y, z) &= g_x(u - x) \\ \Delta g_y(x, y, z) &= g_y(v - y). \end{aligned} \quad (20)$$

Therefore, Δg_x and Δg_ycan be estimated by fitting the pixel-shift data.

Finally, the nonlinearity distributions of the gradient field for g_x and g_y are defined as follows:

$$\begin{aligned}\text{Nonlinearity}_x(x, y, z) &= \left(\frac{\partial G_x}{\partial x}(x, y, z) - g_x\right)\Big/ g_x \\ \text{Nonlinearity}_y(x, y, z) &= \left(\frac{\partial G_y}{\partial x}(x, y, z) - g_y\right)\Big/ g_y. \end{aligned} \quad (21)$$

In addition, the field gradient [mT/m] can be measured using a phantom with known geometry [22]. For example, g_x is calculated using the equation:

$$g_x = \frac{2\pi}{\gamma L_x t_x}, \quad (22)$$

where γ is the gyromagnetic ratio, L_x is the size of the phantom, and t_x is the sampling rate of the sequence. The gradient efficiency [mT/m/A] is calculated by dividing the field gradient by the current value for the readout gradient (gradient current).

3. Materials and methods

The MRI system used in this study consists of a bulk magnet ($B_0 = 4.74$ T, RT bore diameter = 23 mm), an MRI console (MRTechnology, Japan), and an MRI probe. The bulk magnet is comprised of six vertically stacked (120 mm high) annular bulk superconductors (outer diameter (OD) = 60 mm) made of c-axis-oriented single-domain EuBCuO crystals ($T_c = 92$ K), as shown in figure 3(a). The inner diameter (ID) and the thickness of both the upper and lower superconductors were 28 and 23 mm, respectively. The ID and the thickness of the middle four superconductors were 36 and 18.5 mm, respectively. The probe was installed in the RT bore of the bulk magnet. The probe consisted of a twisted-loop radio frequency (RF) coil (ID = 8.1 mm), gradient coils, and an RT

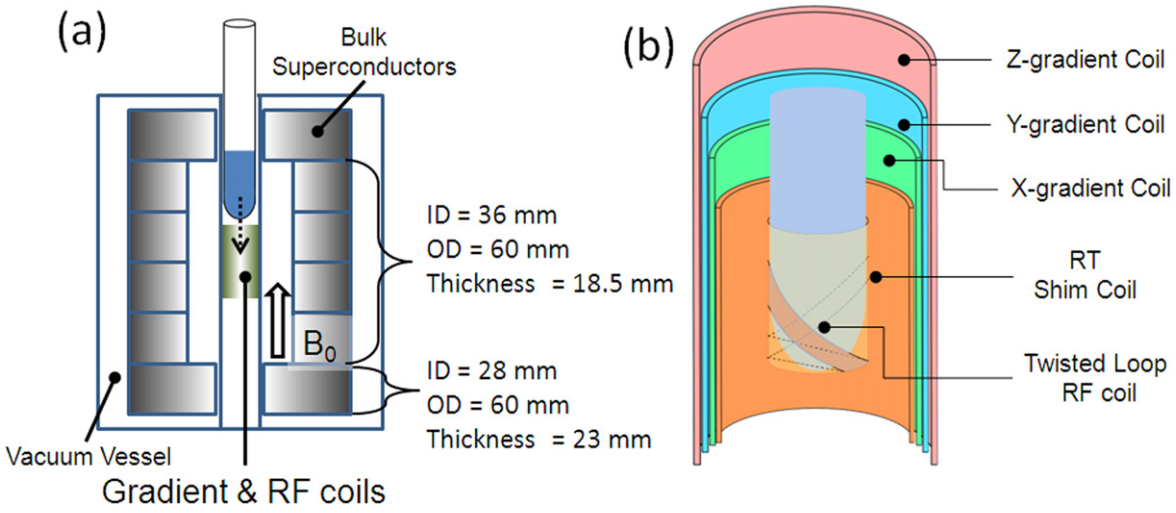

Figure 3. (a) Schematic diagram of the bulk magnet, which consists of six stacked superconductors. (b) Schematic diagram of the probe, which consists of the gradient, shim, and radio frequency (RF) coils.

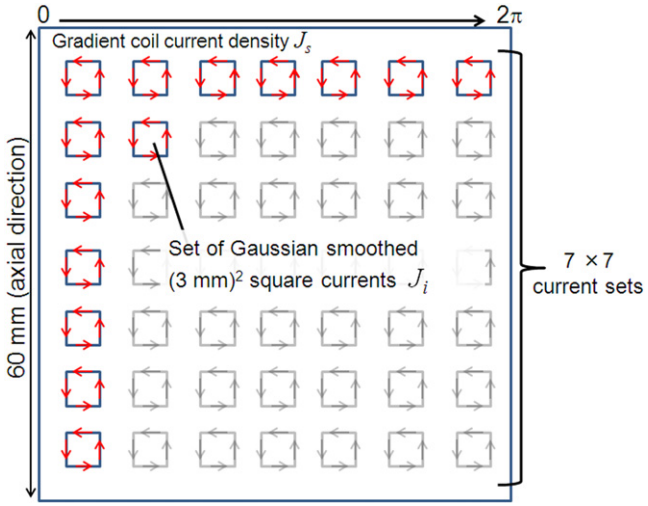

Figure 4. Basic functions comprised of 49 square currents used for the target-field method.

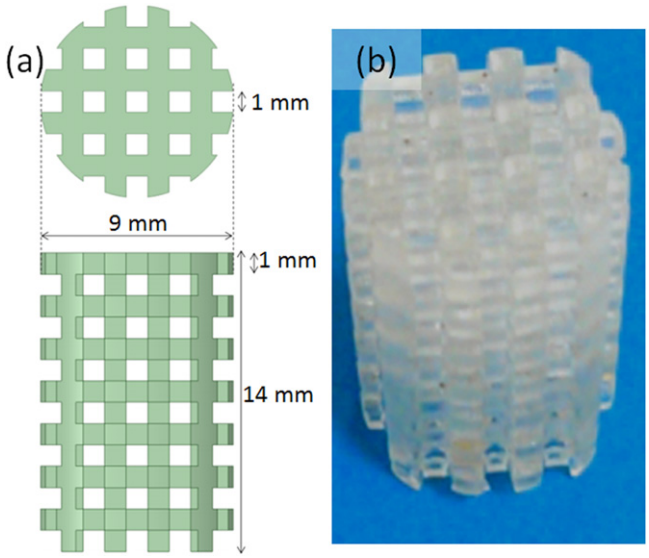

Figure 5. (a) A schematic diagram of the lattice phantom. (b) A fabricated phantom.

shim coil. The diameters of the *x*-, *y*-, and *z*-gradient coils were 21.5, 22.0, and 22.5 mm, respectively. The shim coil (OD = 20.5 mm, ID = 19.0 mm) was located inside the *x*-gradient coil, as shown in figure 3(b).

In this study, the inner (R_1) and outer (R_2) radii used in the simulation of the boundary conditions for the FDM were 18 and 30 mm, respectively. Forty-nine sets of Gaussian smoothed $(3\ \text{mm})^2$ square currents were used as the basis function for the target-field method, as shown in figure 4. The regularization parameter of α was determined by using a trial-and-error process. The gradient fields (target volume = ϕ 9, 10 mm height) along the *x*-, *y*-, and *z*-directions were used as the target field.

The longitudinal (*z*-gradient) and transverse (*x*- and *y*-gradients) gradient coils were designed using our method. The longitudinal coil was fabricated on a plastic tube (thickness = 0.1 mm) using polyethylene-coated Cu wires (0.3 mm diameter). The transverse coil designed in this study was fabricated by cutting the winding patterns on copper sheets (thickness = 0.1 mm) using the commercial CNC cutter (Silhouette Cameo, Graphtech, Japan).

To verify our gradient coil design approach, the gradient efficiencies and the nonlinearity distributions were calculated and measured. The gradient efficiencies (mT/m/A) and the nonlinearity distributions for the *x*- and *z*-gradients were calculated using the FDM. The values were also calculated using the Biot–Savart law without the boundary conditions to show the shielding effect. They were then compared with the efficiencies and nonlinearity distributions measured using the three-dimensional lattice phantom (diameter = 9.0 mm, height = 14.0 mm), as shown in figure 5. The phantom was acquired using the three-dimensional spin echo (3DSE) sequence (TR/TE = 100/10 ms, matrix size = 128^3, voxel size = $100\ \mu\text{m}^3$). The distortion of the MR images was estimated by fitting the pixel-shift data with a third-order

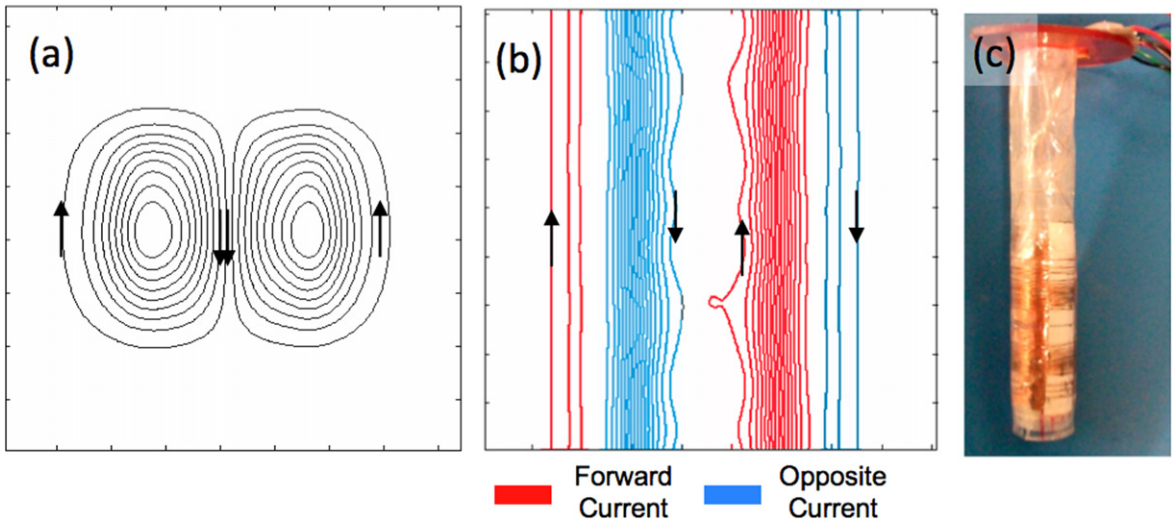

Figure 6. (a) Transverse and (b) longitudinal coil designed in this study. (c) Fabricated gradient coils according to the coil design of (a) and (b).

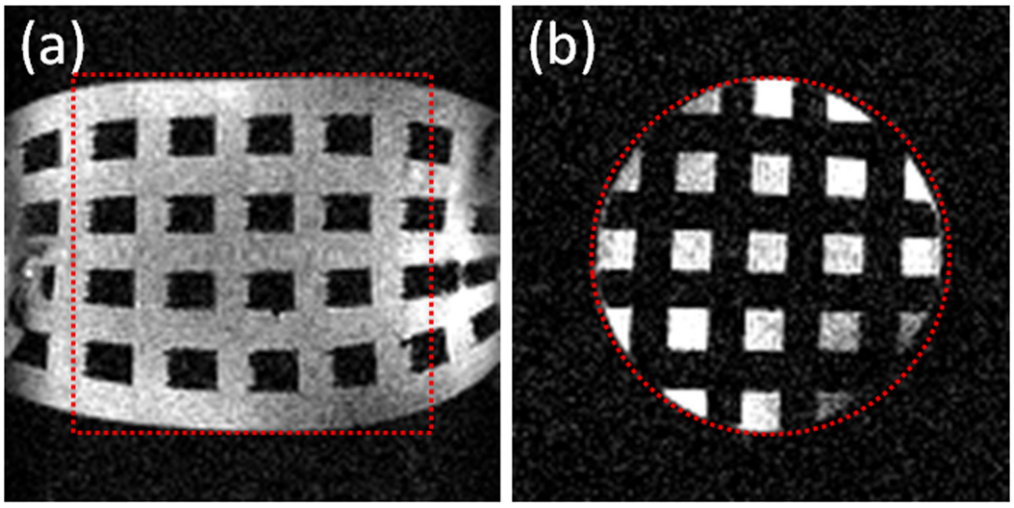

Figure 7. MR images of the lattice phantom (shown in figure 6). Red dashed lines show the area of the target field used in this study.

Table 1. The calculated and measured gradient efficiencies.

	Biot–Savart [mT/m/A]	FDM [mT/m/A]	Measured [mT/m/A]
Transverse (G_x)	55.6	51.6	52.0
Longitudinal (G_z)	84.0	72.4	74.0

polynomial. The nonlinearity distributions and the gradient efficiencies were calculated using equations (21) and (22), respectively.

In addition to the gradient efficiency and nonlinearity, the current dependence of the field gradient strength is the essential factor for the MRI. This is because the encoding scheme for usual MRI systems is implemented based on the assumption that the field gradient strength is proportional to the applied gradient current. If this assumption is not satisfied, the MR images will suffer from signal artifacts and distortion. To show the current dependence of the field gradient strength, the field gradients (mT/m) for the x- and the z-gradient coils were measured with gradient currents of ±3.125, ±2.5, ±1.875, ±1.25, and ±0.625 A. The values were calculated using a 3DSE sequence (TR/TE = 100/10 ms, matrix size = 128^3) and a sphere phantom with a diameter of 6.4 mm.

4. Results and discussion

Figures 6(a) and (b) show the transverse and longitudinal gradient coil winding patterns. The arrows in figures 6(a) and (b) show the current flow in the coils. Figure 6(c) shows the fabricated gradient coil according to the design.

Table 1 shows the calculated and measured gradient efficiencies for the x- and z-gradient coils. The second and third columns of the table show the values of the efficiencies

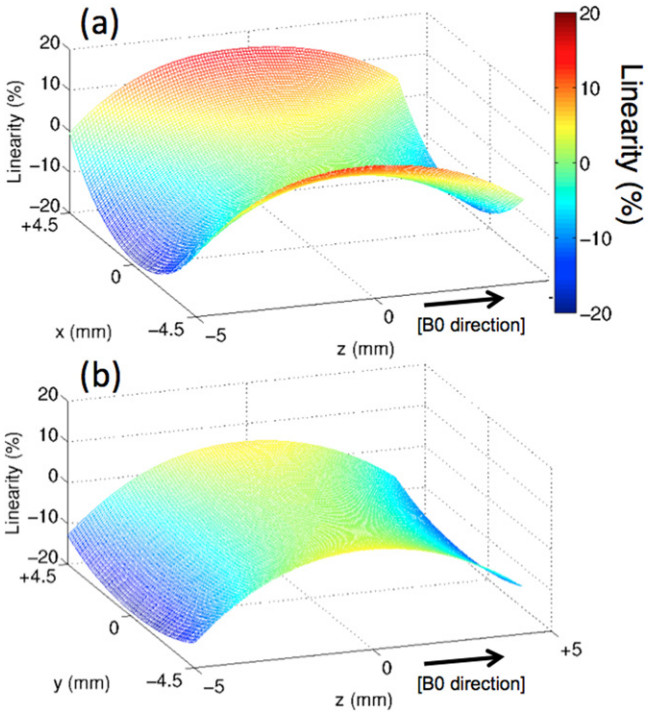

Figure 8. The linearity of the transverse gradient field in the (a) *zx*-plane at $y = 0.0$ mm; in the (b) *zy*- plane at $x = 0.0$ mm. Data were calculated using the FDM.

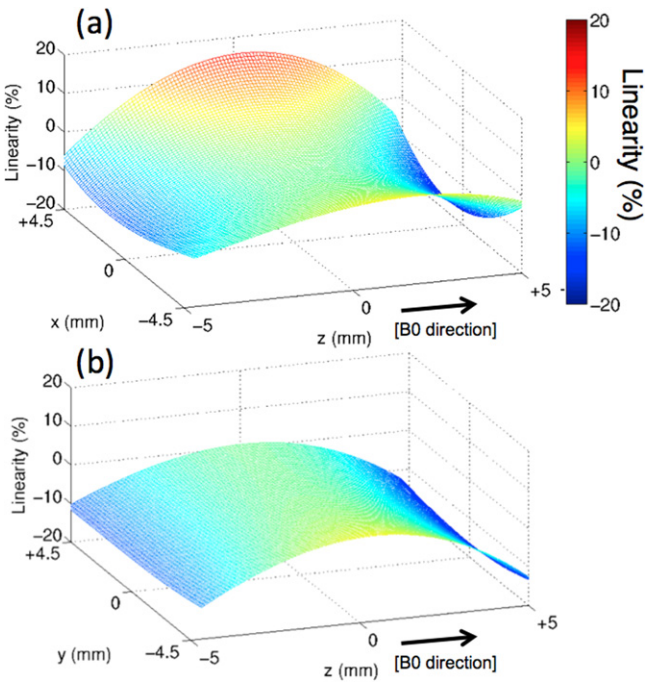

Figure 9. The linearity of the transverse gradient field in the (a) *zx*-plane at $y = 0.0$ mm; in the (b) *zy*-plane at $x = 0.0$ mm. Values were measured using the lattice phantom.

calculated using the Biot–Savart law and the FDM, respectively. The values in the fourth column were measured using the lattice phantom. As clearly shown in the second and fourth column, the calculation results without the boundary conditions were higher than the measured values. On the other hand, the efficiencies calculated using the FDM agreed well with the measured values.

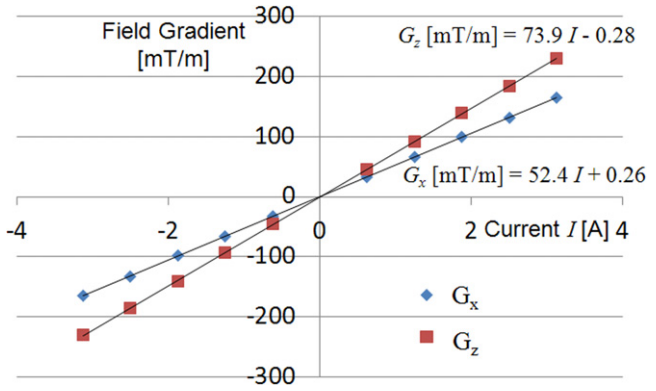

Figure 10. Current dependence for the field gradient of the *x*- and *z*-gradient coils.

Figure 7 shows the MR images of the lattice phantom, shown in figure 6(c), doped in the $CuSO_4$ water. The phantom was acquired without significant distortion inside the target volume, as illustrated by the red dashed lines.

Figure 8 shows the nonlinearity spatial distribution of the *x*-gradient coil, calculated using the FDM. The maximum nonlinearity of the field was 17.4%.

Figure 9 shows the nonlinearity spatial distribution measured using the lattice phantom. The maximum nonlinearity calculated from the measured distribution was 16.8%. The calculated and the measured distributions were in reasonable agreement with each other.

As mentioned above, the field gradient strength should be proportional to the applied current to achieve the correct encoding. Figure 10 shows the current dependence for the field gradient of the *x*- and *z*-gradient coils. The solid lines show the regression lines for the *x*- ($R = 0.999$) and *z*-gradient ($R = 0.999$) coils. The field gradient strength varies linearly with the gradient current.

The other solution to avoid the shielding problem is to use the active shielding coil [23]. However, additional space for the coil will be required. In this case, it is challenging to install the coil in the magnet with a small bore size, such as the bulk magnet.

The *z*-gradient coil winding pattern shown in figure 6(b) seems irregular, because the design algorithm did not consider the symmetricity of the winding pattern in this study. Therefore, it is possible to design simpler patterns using the symmetry condition. In addition to this, the larger number of square currents will give smoother winding patterns. Furthermore, the gradient coils developed in this paper were not exactly as designed, owing to fabrication error. This is because the fabricated coils and copper wires were very small, and, therefore, the coil design becomes sensitive to the fabrication errors. The error gives rise to undesirable components of the field, such as asymmetricity of the distribution.

The nonlinearity of the gradient coils developed in this study is larger than commercially available gradient coils. Because of the small bore diameter, there are some limitations in designing the gradient coils to achieve the practical design,

such as the coil diameter and the number of wire turns. In the future, these limitations will be solved by using larger bulk superconductors, although it is still difficult to make large superconducting crystals.

5. Conclusion

In this paper, we proposed a new gradient coil design method for the bulk magnet using the target-field method and the FDM. The winding patterns for the transverse and longitudinal coils were designed and developed by considering the boundary conditions. The nonlinearity distribution and the efficiency of the coils, measured using the lattice phantom, were in good agreement with the calculation results. In addition to this, a proportional relationship between the field gradient strength and the gradient current was observed.

We conclude that these results demonstrate the accuracy and the effectiveness of our approach. Our approach enabled a gradient coil design under the condition of the flux shielding property. As a result, optimization of various types of gradient coils for the bulk magnet will be available. Although this study offered experiments concerning the bulk magnet, we hope that our approach will contribute the gradient coil design for other types of HTS magnets.

Acknowledgments

We would like to thank Editage (www.editage.jp) for English language editing. Takeshi Kimura (Ohtsuka, Inc., Tsukuba, Japan) gave insightful comments and suggestions about the fabrication of the gradient coils.

References

[1] Terao Y, Ozaki O, Ichihara C, Kawashima S, Hase T, Kitaguchi H and Fukuyama H 2013 Newly designed 3 T MRI magnet wound with Bi-2223 tape conductors *IEEE Trans. Appl. Supercond.* **23** 4400904

[2] Slade R A, Parkinson B J and Walsh R M 2014 Test results for a 1.5 T MRI system utilizing a cryogen-free YBCO magnet *IEEE Trans. Appl. Supercond.* **24** 1–5

[3] Maeda H and Yanagisawa Y 2014 Recent developments in high-temperature superconducting magnet technology (review) applied superconductivity *IEEE Trans. Appl. Supercond.* **24** 1–12

[4] Nakamura T, Itoh Y, Yoshikawa M, Oka T and Jun U 2007 Development of a superconducting magnet for nuclear magnetic resonance using bulk high-temperature superconducting materials *Concepts Magn. Reson.* B **31** 65–70

[5] Ogawa K, Nakamura T, Terada Y, Kose K and Tomoyuki H 2011 Development of a magnetic resonance microscope using a high Tc bulk superconducting magnet *Appl. Phys. Lett.* **98** 234101

[6] Hahn S, Ahn M, Bascunan J, Yao W and Iwasa Y 2009 Nonlinear behavior of a shim coil in an LTS/HTS NMR magnet with an HTS insert comprising double-pancake HTS-tape coils *IEEE Trans. Appl. Supercond.* **19** 2285–8

[7] Yanagisawa Y, Piao R, Iguchi S, Nakagom H, Takao T, Kominato K and Maeda H 2014 Operation of a 400 MHz NMR magnet using a (RE: Rare Earth) Ba_2 Cu_3 O_{7-x} high-temperature superconducting coil: towards an ultra-compact super-high field NMR spectrometer operated beyond 1 GHz *J. Magn. Reson.* **249** 38–48

[8] Ahn M, Jang J, Hahn S, Kim Y and Lee H 2014 Field mapping and automated shimming of an HTS magnet by 'internal' active shim coils located in the bore of the magnet *IEEE Trans. Appl. Supercond.* **25** 4300804

[9] Tamada D, Nakamura T, Itoh Y and Kose K 2013 Experimental evaluation of the magnetization process in a high Tc bulk superconducting magnet using magnetic resonance imaging *Physica* C **492** 174–7

[10] Poole C P, Datta T and Farach H A 1988 *Copper Oxide Superconductors* (New York: Wiley)

[11] Fossheim K and Sudbø A 2005 *Superconductivity: Physics and Applications* (Chichester: Wiley)

[12] Turner R 1993 Gradient coil design: a review of methods *Magn. Reson. Imaging* **11** 903–20

[13] Turner R 1986 A target field approach to optimal coil design *J. Phys. D: Appl. Phys.* **19** L147

[14] Turner R 1988 Minimum inductance coils *J. Phys. E: Sci. Instrum.* **21** 948

[15] Jin J 1998 *Electromagnetic Analysis and Design in Magnetic Resonance Imaging* (Boca Raton, FL: CRC Press)

[16] Forbes L K and Crozier S 2001 A novel target-field method for finite-length magnetic resonance shim coils: I. zonal shims *J. Phys. D: Appl. Phys.* **34** 3447

[17] Liu W, Zu D, Tang X and Guo H 2007 Target-field method for MRI biplanar gradient coil design *J. Phys. D: Appl. Phys.* **40** 4418

[18] Strikwerda J C *Finite Difference Schemes and Partial Differential Equations* (Belmont, CA: Wadsworth & Brooks/Coles)

[19] Zhu M, Xia L, Liu F, Zhu J, Kang L and Crozier S 2012 A finite difference method for the design of gradient coils in MRI—an initial framework *IEEE Trans. Biomed. Eng.* **59** 2412–21

[20] Kawanaka A and Takagi M 1986 Estimation of static magnetic field and gradient fields from NMR image *J. Phys. E: Sci. Instrum.* **19** 871

[21] Wang D, Doddrell D M and Cowin G 2004 A novel phantom and method for comprehensive 3-dimensional measurement and correction of geometric distortion in magnetic resonance imaging *Magn. Reson. Imaging* **22** 529–42

[22] Bernstein M A, King K F and Zhou X J 2004 *Handbook of MRI Pulse Sequences* (London: Elsevier)

[23] Mansfield P and Chapman B 1969 Active magnetic screening of gradient coils in NMR imaging *J. Magn. Reson.* **66** 573–6